A micrometre-sized heat engine operating between bacterial reservoirs

Sudeesh Krishnamurthy[1], Subho Ghosh[2], Dipankar Chatterji[2], Rajesh Ganapathy[3,4] and A. K. Sood[1,3]★

Artificial microscale heat engines are prototypical models to explore the mechanisms of energy transduction in a fluctuation-dominated regime[1,2]. The heat engines realized so far on this scale have operated between thermal reservoirs, such that stochastic thermodynamics provides a precise framework for quantifying their performance[3–6]. It remains to be seen whether these concepts readily carry over to situations where the reservoirs are out of equilibrium[7], a scenario of particular importance to the functioning of synthetic[8,9] and biological[10] microscale engines and motors. Here, we experimentally realize a micrometre-sized active Stirling engine by periodically cycling a colloidal particle in a time-varying optical potential across bacterial baths characterized by different degrees of activity. We find that the displacement statistics of the trapped particle becomes increasingly non-Gaussian with activity and contributes substantially to the overall power output and the efficiency. Remarkably, even for engines with the same energy input, differences in non-Gaussianity of reservoir noise results in distinct performances. At high activities, the efficiency of our engines surpasses the equilibrium saturation limit of Stirling efficiency, the maximum efficiency of a Stirling engine where the ratio of cold to hot reservoir temperatures is vanishingly small. Our experiments provide fundamental insights into the functioning of micromotors and engines operating out of equilibrium.

In a seminal experiment, Blickle and Bechinger[3] devised a micrometre-sized Stirling heat engine that was driven by fluctuations from an equilibrium thermal reservoir, while being subject to time-dependent potentials in an optical trap. Like its macroscopic counterpart, the mean quasistatic efficiency of such an engine (approximately 14% for a colloidal bead in water) is given by $\mathcal{E}_\infty = \mathcal{E}_c[1 + \mathcal{E}_c/\ln[(k_{max}/k_{min})]]^{-1}$. Here, $\mathcal{E}_c = 1 - (T_C/T_H)$ is the Carnot efficiency, T_C and T_H are the cold and hot reservoir temperatures, respectively, and the ratio of trap stiffnesses (k_{max}/k_{min}) is analogous to the compression ratio of a macroscopic engine. By imposing an external source of noise on the trapped colloidal particle, corresponding to an effective T_H of nearly 3,000 K (ref. 11), and implementing the microscopic equivalent of an adiabatic process, a Brownian Carnot engine with higher power output and efficiency was later realized[4]. Although strategies for harnessing the work done by these microscale heat engines have not yet been devised, these studies underscore the feasibility of using a colloidal particle as the working substance of a heat engine to elucidate the role of fluctuations on its performance. In microscale heat engines investigated hitherto, noise fluctuations associated with the reservoirs decorrelate on a timescale that is much smaller than that associated with the working substance—the Brownian time of the colloidal bead. Owing to this separation of timescales, particle dynamics in such reservoirs follow Gaussian statistics and equilibrium stochastic thermodynamics can be readily applied. However, in a bath of active particles—a canonical athermal reservoir, noise fluctuations can remain temporally correlated for substantially longer[12]. This results in the breakdown of the fluctuation–dissipation theorem[13,14] and, as a consequence, particle dynamics in active reservoirs follow non-Gaussian statistics over suitable time and length scales[15,16]. Importantly, while stochastic thermodynamics models show that between athermal reservoirs with identical noise intensities (that is, temperatures), heat flow is still possible due to a difference in the non-Gaussianity of their noises[17,18], whether work can also be extracted remains unclear. Moving outside the realm of stochastic thermodynamics, quantum analogues of classical heat engines[19–22] coupled to athermal reservoirs are predicted to operate at efficiencies that surpass the equilibrium Carnot efficiency[23,24]. In light of these theoretical advances, a natural step forward would be the experimental realization of microscale heat engines that exploit features unique to athermal reservoirs for extracting work.

Here we designed, constructed and quantified the working of an active heat engine. A 5 μm colloidal bead, held in a harmonic optical trap, in a suspension of motile bacteria—*Bacillus licheniformis*—acts as the working substance. The time-dependent variations in laser intensity, that is, trap strength, mimic the role of the piston of a macroscopic engine. A key advantage of utilizing a bacterial reservoir is that bacterial metabolism and the corresponding activity are strongly sensitive to the bath temperature[25,26]. We exploit this behaviour and periodically create conditions of high and low activity, thus imitating passive reservoirs with a temperature difference (see Methods and Supplementary Text and Supplementary Figs 1 and 2). The bacterial activity depends on a host of physico-chemical parameters and was found to be exclusive to each experiment. This allowed us to access reservoirs with different activities, while keeping the bacterial number density constant. We parametrized bacterial activity by an active temperature, $k_B T_{act} = (1/2)k_x \langle x^2 \rangle + (1/2)k_y \langle y^2 \rangle$ (refs 16,27). Here, k_x, x and k_y, y are trap stiffness and the displacement of the bead from the trap centre, respectively, along the x and y directions. The engine is driven by fluctuations arising from the differences in bacterial activity across the reservoirs, ΔT_{act}, and we execute the microscopic equivalent of a Stirling cycle.

The active Stirling cycle executed by the engine, as outlined in Fig. 1, is analogous to its passive counterpart[3], except here, the activity of the bath is maintained constant during the

---

[1]Department of Physics, Indian Institute of Science, Bangalore - 560012, India. [2]Molecular Biophysics Unit, Indian Institute of Science, Bangalore - 560012, India. [3]International Centre for Materials Science, Jawaharlal Nehru Centre for Advanced Scientific Research, Jakkur, Bangalore - 560064, India. [4]Sheikh Saqr Laboratory, Jawaharlal Nehru Centre for Advanced Scientific Research, Jakkur, Bangalore - 560064, India. *e-mail: asood@physics.iisc.ernet.in
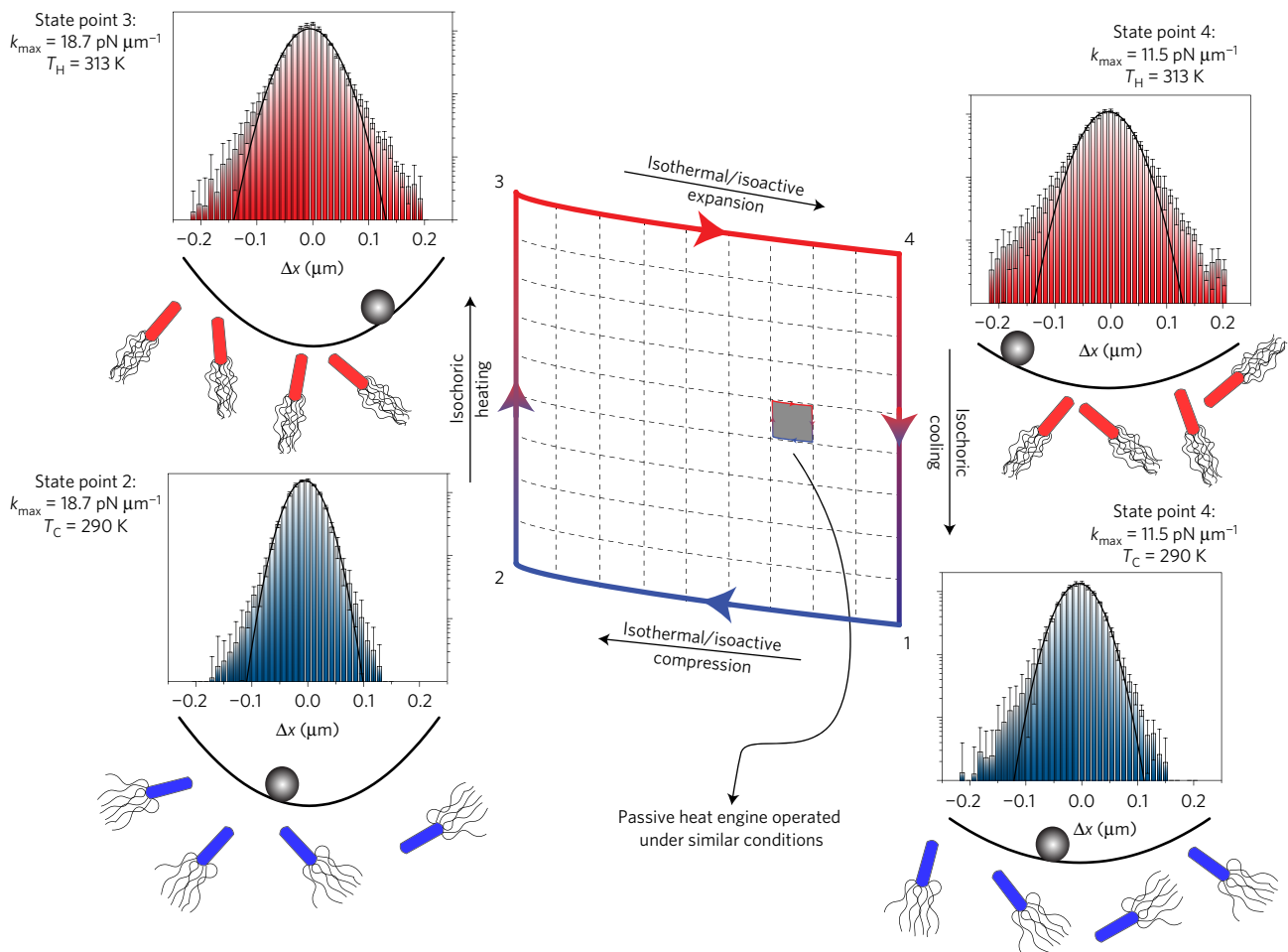
Figure 1 | Micrometre active Stirling engine. A Stirling cycle consists of isothermal compression (1 → 2) and expansion (3 → 4) steps at temperatures T_C and T_H, respectively, connected by isochores 2 → 3 and 4 → 1. In the active Stirling engine, for large activities, a substantial contribution to the total work stems from bacterial activity, and the isotherms can be effectively replaced by isoactivity lines. Increasing (decreasing) the trap stiffness decreases (increases) the phase space volume available to the colloidal particle and mimics a compression (expansion) stroke of a macroscopic Stirling engine. $P(\Delta x)$ at state points 3 and 4 are substantially more non-Gaussian than at state points 1 and 2 due to increased bacterial activity. The black lines represent Gaussian fits. The error bars represent standard error of the mean (SEM) from four independent realizations of the engine with different bacterial samples of approximately the same ΔT_{act}. The area of the large(small) Stirling cycle represents the average work done by the active(passive) engine as it executes one Stirling cycle.

isothermal processes (1 → 2 & 3 → 4), while k_x and k_y are linearly increased(decreased) to mimic compression(expansion) of the system. The isochoric processes (2 → 3 & 4 → 1) now correspond to changing the activity while maintaining k_x and k_y constant (see Methods). The compression/expansion of the trap as well as the change in activity is captured by the probability distributions in the x-position, $P(\Delta x)$, of the colloidal bead. Owing to non-equilibrium fluctuations, $P(\Delta x)$ shows strong non-Gaussian behaviour. The position of the colloidal bead represents the state of the system as the cyclic process described in Fig. 1 is steadily executed and thermodynamic quantities were computed using the framework of stochastic thermodynamics[6,28]. Since fluctuations in our system follow non-Gaussian statistics, T_{act} cannot be used to define thermodynamic quantities. As per the definition, T_{act} is the temperature of an equilibrium reservoir with the same average potential energy $\langle U \rangle$ as the trapped bead in our bacterial reservoir. Thus, the equilibrium reservoir at T_{act} and our bacterial reservoir transfer the same amount of heat during an isochoric process.

We first compared the performance of an active engine with a passive one (see Supplementary Movies 1 and 2). For the highest activity accessible in our experiments, the work done per cycle, W_{cycle}, of the active engine, represented by the area of the larger

Stirling cycle in Fig. 1, is about two orders of magnitude larger than that of the passive engine (see Supplementary Figs 5 and 6). A comparison of heat engines is possible only in the quasistatic limit (cycle duration $\tau \to \infty$) or at peak power output (see Methods). Here we operate our engines in the quasistatic limit. In the quasistatic limit, the instantaneous $P(\Delta x)$ of the colloidal particle should mimic the closing (1 → 2) and opening (3 → 4) of the optical trap. This implies, $k(t_1)\langle \Delta x^2(t_1) \rangle = k(t_2)\langle \Delta x^2(t_2) \rangle = k_B T$, where t_1 and t_2 denote any two time instances along the isotherms. Thus, the $P(\Delta x)$ values (determined over suitably small time bins), when appropriately scaled, should collapse, and this is indeed observed for $\tau = 22$ s (Fig. 2a) (see also Supplementary Fig. 7). The engines are thus operating in the quasistatic limit, which enables a direct comparison of engine performance across activities.

In Fig. 2b, we show the cumulative work done, in units of $k_B T_C (T_C = 290 \text{ K})$, at the end of each Stirling cycle by the passive engine (filled symbols) and the active engine (open symbols), for various values of ΔT_{act}. The error bars for each ΔT_{act} are obtained from multiple experimental realizations and represent the standard error of the mean (SEM) (see Supplementary Fig. 5). Since the work is cumulative, so is the error. The slopes of the trajectories are negative, and work is done by the engine on the surroundings.
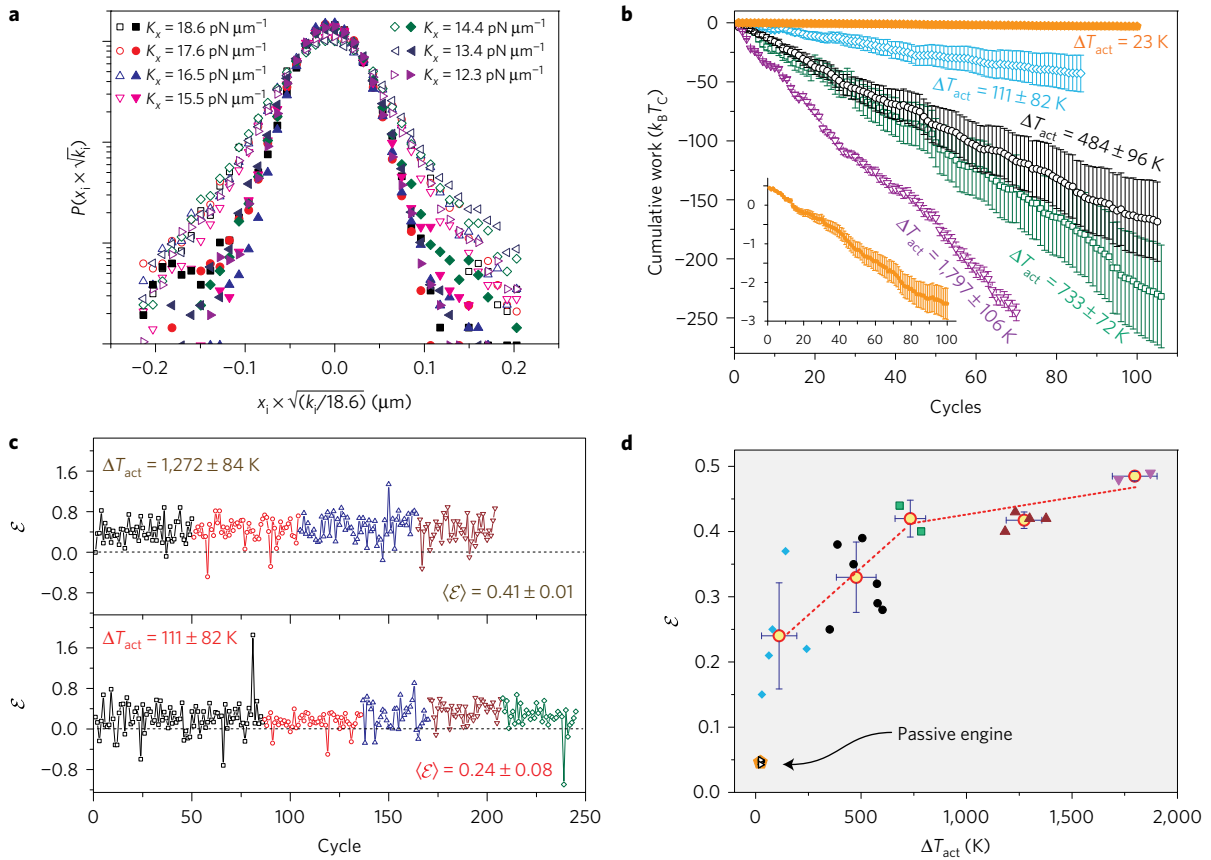
Figure 2 | Comparison of active engines at different activities. a, Scaled $P(\Delta x)$ values at different instances along the isothermal expansion stroke (3→4) for two different activities. $\Delta T_{act} = 63\,K$ (filled symbols) and $\Delta T_{act} = 1,299\,K$ (open symbols). **b**, Cumulative work done by active (open symbols) and passive (filled symbols) engine for different values of ΔT_{act}. The error bars represent standard error of the mean obtained from multiple realizations for approximately the same ΔT_{act} and are cumulative. Inset to **b** shows work done by the passive engine on a scale where fluctuations are visible. **c**, Fluctuations in efficiency of the active engine as the Stirling cycle is continuously executed for two values of ΔT_{act}. The different colours and symbols represent individual realizations for each ΔT_{act}. **d**, Average efficiency of the active engine (red circles) and the passive engine (orange pentagon) estimated from multiple experimental realizations for approximately the same ΔT_{act}. The x and y-error bars correspond to SEM of ΔT_{act} and $\mathcal{E}$, respectively. The symbol colour and shape corresponds to individual realizations that have nearly the same ΔT_{act}.

With increasing activity, the cumulative work steadily increases (Fig. 2b) and, at the highest activities investigated, ΔT_{act} is in excess of 1,200 K. Such enormous differences in reservoir temperatures are impossible to mimic in passive microengines without an external source of noise[11]. W_{cycle} is a fluctuating quantity due to the stochastic nature of the engine, and so is the efficiency, $\mathcal{E}_{cycle}$. Figure 2c shows these fluctuations for multiple realizations of active engines corresponding to $\Delta T_{act} = 1,272 \pm 84\,K$ (top panel) and $111 \pm 82\,K$ (bottom panel), respectively. In Fig. 2d, the open triangles and filled symbols represent $\langle \mathcal{E}_{cycle} \rangle$ for individual realizations of the passive and active heat engine, respectively. The red circles denote efficiency $\mathcal{E}$ averaged over active engines with nearly the same ΔT_{act} (shown by similar symbols). Most remarkably, at the highest activity, $\mathcal{E}$ of the bacterial engine is almost an order of magnitude larger than its passive counterpart, and is only a factor of two smaller than biological motors[10]. Experiments carried out at a different k_{max} and k_{min}, but with same (k_{max}/k_{min}), showed similar trends in both work and efficiency (see Supplementary Information).

For equilibrium engines operating in the quasistatic limit, the work done per cycle is given by $W_q = 2k_B T_C [1 - (T_H/T_C)] \ln\sqrt{(k_{max}/k_{min})}$. W_q and $\mathcal{E}_q$ for the passive engine, represented by open inverted triangles in Fig. 3a,b, closely match the experimental values (filled pentagons) and reaffirm that we are operating the engine in the quasistatic limit. Turning our attention to the active engines, we find that while W increases steadily with ΔT_{act} (Fig. 3a),

$\mathcal{E}$ increases and then shows a tendency to saturate at high ΔT_{act} (Fig. 3b, and Supplementary Fig. 5). Such a behaviour is typical of an equilibrium Stirling engine, where the quasistatic efficiency saturates to $\mathcal{E}_{sat} = (1 + 1/\ln(k_{max}/k_{min}))^{-1}$ as $T_C/T_H \to 0$, represented by the solid horizontal line in Fig. 3b. The experimentally determined efficiencies surpass this limit, suggesting a failure of the equilibrium description in evaluating $\mathcal{E}_{sat}$ for the active engines.

To understand the origin(s) of such high $\mathcal{P}$ and $\mathcal{E}$ of our active engines, we carefully examined the fluctuations of the trapped colloidal particle in the active reservoirs. $P(\Delta x)$ in the hot(cold) reservoir for $\Delta T_{act} = 1,272 \pm 84\,K$ is shown by the red(blue) histogram in Fig. 3c. The green line represents a Gaussian fit to $P(\Delta x)$. To isolate the contributions from Gaussian fluctuations to the total W and $\mathcal{E}$, we simulated Stirling cycles by drawing particle displacements at random from the Gaussian region alone (green shaded area). A cumulative sum of these displacements yielded particle trajectories using which, the work done, W^G and the efficiency, $\mathcal{E}^G$ were calculated (see Supplementary Information). For such a Gaussian engine, an effective temperature T_{eff} can be precisely defined and $\Delta T_{eff} < \Delta T_{act}$ (top x-axis in Fig. 3a,b) since we have chosen only the low-energy contributions to $\langle U \rangle$. $\langle W^G \rangle$ and $\langle \mathcal{E}^G \rangle$ for the simulated Gaussian engine are shown as green circles in Fig. 3a and b, respectively. Strikingly, at the highest activity, 57% of total W and 55% of the total $\mathcal{E}$ are due to non-Gaussian fluctuations. In fact, these fluctuations account for ~59% of the potential energy
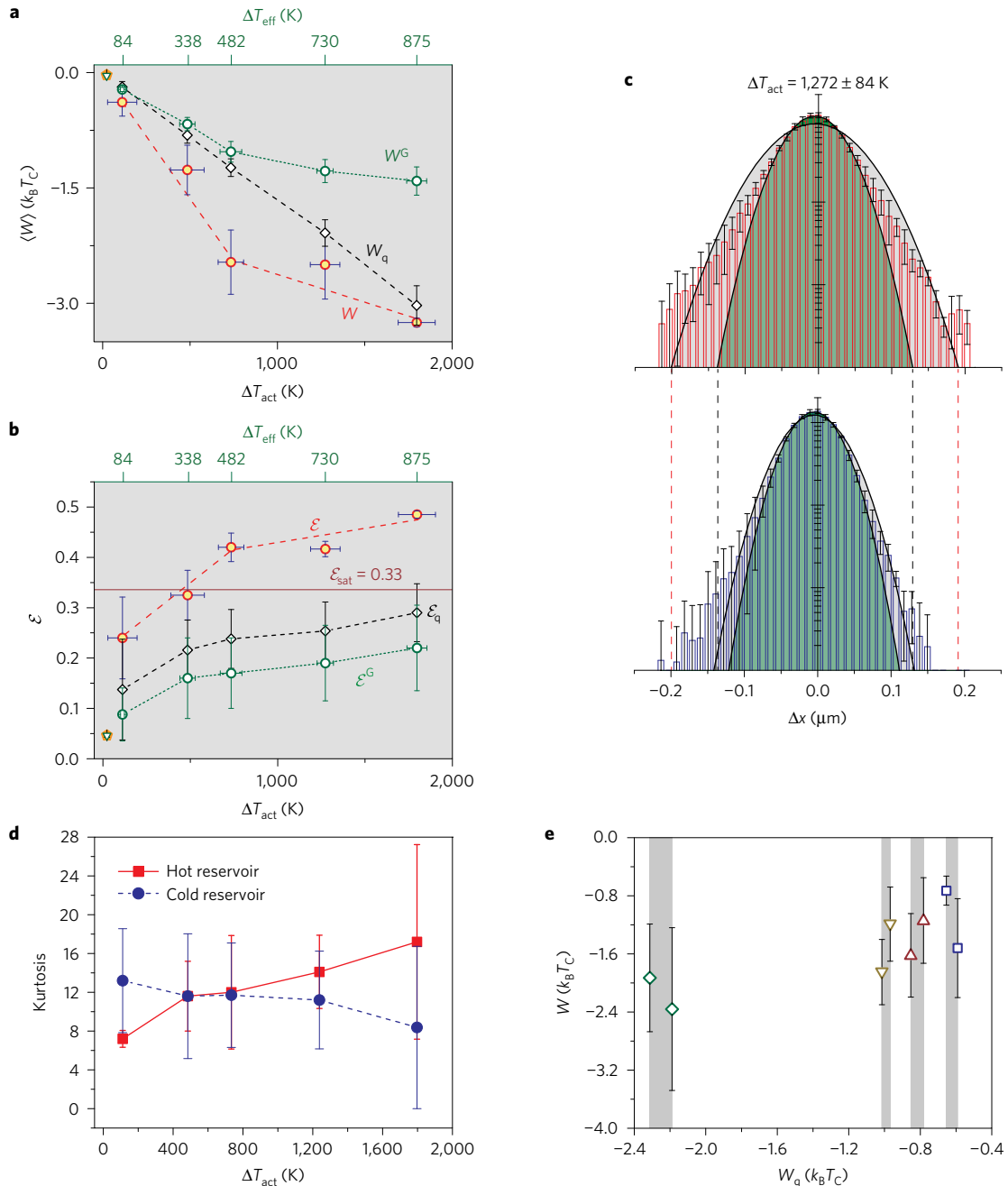
Figure 3 | Elucidating the origins of active engine performance. a,b, Work done (**a**) and efficiency (**b**) for the experimental and simulated engines, respectively. The red lines are only a guide to the eye. Experimental and calculated W and $\mathcal{E}$ for passive engines are represented by a filled pentagon and open inverted triangle, respectively. Solid circles represent an experimental active engine, open circles represent a simulated Gaussian engine and diamonds represents the quasistatic Stirling engine. The efficiency of passive engines saturates for $T_C/T_H \rightarrow 0$ at $\mathcal{E}_{sat}$ represented by the brown line in **b**. **c**, Experimental $P(\Delta x)$ values at trap stiffness, $k = k_{min}$, in the hot (red bars) and cold (blue bars) reservoirs for $\Delta T_{act} = 1,272 \pm 84$ K. The green line represents the Gaussian fit to the data and the fluctuations in the green shaded region alone contribute to W^G and $\mathcal{E}^G$ (green circles in **a** and **b**). The black line represents a Gaussian engine with the same variance as the experimental active engine and is an overlay. Fluctuations within the grey shaded area contribute to W_q and $\mathcal{E}_q$. **d**, Average kurtosis of $P(\Delta x)$ for hot(red squares) and cold(blue circles) reservoirs for different values of ΔT_{act}. In **a**–**d**, the x and y-error bars correspond to the SEM of the respective quantities obtained from multiple realizations. **e**, Work, W, done by active engines versus work done by a Gaussian engine with the same variance, W_q. Points that lie within the grey bars correspond to engines with approximately the same ΔT_{act} and hence the same W_q. The average experimental work, however, differs due to differences in non-Gaussian statistics. The error bars represent the standard deviation within an individual realization.

difference between the hot and cold reservoirs (Fig. 3c), explaining their large contribution to W (see Methods).

We can further compare the experimental active engine with a passive engine operating between equilibrium reservoirs at the same $\langle \Delta U \rangle$, that is, the same ΔT_{act}. The solid black curve in Fig. 3c represents a Gaussian with width equal to the variance of $P(\Delta x)$ of the active engine. The black diamonds in Fig. 3a and b show W_q and $\mathcal{E}_q$, respectively, for a quasistatic equilibrium Stirling engine operating under such conditions. W_q and $\mathcal{E}_q$ continue to remain smaller than W and $\mathcal{E}$ of the corresponding active engine. For

$\Delta T_{act} = 1{,}272 \pm 84$ K, 20% of the contribution to the total work done stems from a few large displacements seen outside of the grey shaded area of the Fig. 3c. These fluctuations comprise about 21% of the difference in U between the $P(\Delta x)$ of the hot and cold reservoirs. For intermediate activities, these large displacements contribute as much as 50% to the total work. We quantified the non-Gaussianity of the distributions, by examining the kurtosis for various bacterial activities (Fig. 3d). The squares and circles in Fig. 3d represent the kurtosis of $P(\Delta x)$ at state points 4 and 1 of the Stirling cycle (see Fig. 1), respectively. The observed increase in the difference in kurtosis between the hot and cold reservoirs confirms that the superior performance of the active engine vis-á-vis equilibrium/Gaussian engines stems entirely from non-Gaussian statistics. Further, while the experimental errors in estimating $\langle W_{cycle} \rangle$ and $\langle \mathcal{E}_{cycle} \rangle$ for passive engines is small, differences in kurtosis for individual realizations with similar ΔT_{act} result in a larger spread in these quantities for active engines. Most remarkably, even for engines with the same ΔT_{act}, that is, the same W_q, the experimental work done is different (Fig. 3e). This implies that work can be extracted due to differences in the statistics alone even when the noise intensities of the reservoirs remain the same.

Collectively, our results show that active engines significantly outperform passive engines, which are bound by the laws of thermodynamics. While one would naively interpret such a result as an outcome of continuous energy input, our experiments demonstrate that the superior performance of active engines arises from access to temporal regimes dominated by non-Gaussian statistics. Our results show that, despite being rare, the non-Gaussian fluctuations[15,16] in position and hence velocity (that is, departure from the equipartition theorem) contribute significantly to the performance and should be explicitly taken into account in future theories. Given that biological motors are known to operate under isothermal conditions[10], it is tempting to speculate if the mechanisms expounded here are also the source of their observed high efficiencies. In view of the recent advances in the fabrication of synthetic self-propelled colloids[29] that can be rendered active by light fields, for example, active reservoirs should be an integral part of the design of future microscopic heat engines that can potentially power microscale and nanoscale electro-mechanical devices.

Methods

Methods, including statements of data availability and any associated accession codes and references, are available in the online version of this paper.

Received 11 January 2016; accepted 29 July 2016; published online 29 August 2016

References

1. Horowitz, J. M. & Parrando, J. M. R. A Stirling effort. *Nat. Phys.* **8,** 108–109 (2012).
2. Hangii, P. & Marchesoni, F. Artificial Brownian motors: controlling transport on the nanoscale. *Rev. Mod. Phys.* **81,** 387–442 (2009).
3. Blickle, V. & Bechinger, C. Realization of micrometer sized stochastic heat engine. *Nat. Phys.* **8,** 143–146 (2012).
4. Martinez, I. A. *et al.* Brownian Carnot engine. *Nat. Phys.* **12,** 67–70 (2016).
5. Sekimoto, K. Langevin equation and thermodynamics. *Prog. Theor. Phys. Suppl.* **130,** 17–27 (1998).
6. Seifert, U. Stochastic thermodynamics, fluctuation theorems and molecular machines. *Rep. Prog. Phys.* **75,** 126001 (2012).
7. Das, S., Narayan, O. & Ramaswamy, S. Ratchet for energy transport between identical reservoirs. *Phys. Rev. E* **66,** 050103 (2002).
8. Browne, W. R. & Feringa, B. L. Making molecular machines work. *Nat. Nanotech.* **1,** 25–35 (2006).
9. Balzani, V. *et al.* Artificial molecular machines. *Angew. Chem. Int. Ed.* **39,** 3348–3391 (2000).
10. Howard, J. *Mechanics of Motor Proteins and the Cytoskeleton* (Sinauer Associates Sunderland, 2001).
11. Martinez, I. A., Roldan, E., Parrando, J. M. R. & Petrov, D. Effective heating to several thousand kelvins of an optically trapped sphere in a liquid. *Phys. Rev. E* **87,** 032159 (2013).
12. Soni, G. V., Jaffar Ali, B. M., Hatwalne, Y. & Shivshankar, G. V. Single particle tracking of correlated bacterial dynamics. *Biophys. J.* **84,** 2634–2637 (2003).
13. Wu, X. L. & Libchaber, A. Particle diffusion in a quasi-two-dimensional bacterial bath. *Phys. Rev. Lett.* **84,** 3017 (2001).
14. Chen, D. T. N. *et al.* Fluctuations and rheology in active bacterial suspensions. *Phys. Rev. Lett.* **99,** 148302 (2007).
15. Tailleur, J. & Cates, M. E. Sedimentation, trapping, and rectification of dilute bacteria. *Euro. Phys. Lett.* **86,** 60002 (2008).
16. Maggi, C. *et al.* Generalized energy equipartition in harmonic oscillators driven by active baths. *Phys. Rev. Lett.* **113,** 238303 (2014).
17. Kanazawa, K., Sagawa, T. & Hayakawa, H. Stochastic energetics of non-Gaussian processes. *Phys. Rev. Lett.* **108,** 210601 (2012).
18. Kanazawa, K., Sagawa, T. & Hayakawa, H. Heat conduction induced by non-Gaussian athermal fluctuations. *Phys. Rev. E* **87,** 052124 (2013).
19. Scully, M. O., Zubairy, S. M., Agarwal, G. S. & Walther, H. Extracting work from a single heat bath via vanishing quantum coherence. *Science* **299,** 862–864 (2003).
20. Koski, J. V., Maisi, V. F., Pekola, J. P. & Averin, D. V. Experimental realization of a Szilard engine with a single electron. *Proc. Natl Acad. Sci. USA* **111,** 13786–13789 (2014).
21. Abah, O. *et al.* Single-ion heat engine at maximum power. *Phys. Rev. Lett.* **109,** 203006 (2012).
22. Dechant, A., Kiesel, N. & Lutz, E. All-optical nanomechanical heat engine. *Phys. Rev. Lett.* **114,** 183602 (2015).
23. Lutz, E. & Abah, O. Efficiency of heat engines coupled to non-equilibrium reservoirs. *Euro. Phys. Lett.* **106,** 20001 (2014).
24. Rossnagel, J., Abah, O., Schmidt-Kaler, F., Singer, K. & Lutz, E. Nanoscale heat engine beyond Carnot limit. *Phys. Rev. Lett.* **112,** 030602 (2014).
25. Shneider, W. R. Jr & Doetsch, R. N. Temperature effects on bacterial movement. *Appl. Environ. Microbiol.* **34,** 695–700 (1977).
26. Lewis, P. & Ford, R. M. Temperature-sensitive motility of *Sulfolobus acidocaldarius* influences population distribution in extreme environments. *J. Bacteriol.* **181,** 4020–4025 (1999).
27. Palacci, J., Cottin-Bizonne, C., Ybert, C. & Bocquet, L. Sedimentation and effective temperature of active colloidal suspensions. *Phys. Rev. Lett.* **105,** 088304 (2010).
28. Blickle, V., Speck, T., Helden, L., Seifert, U. & Bechinger, C. Thermodynamics of a colloidal particle in a time-dependent nonharmonic potential. *Phys. Rev. Lett.* **96,** 070603 (2006).
29. Aranson, I. S. Active colloids. *Phys. Uspekhi.* **56,** 79–92 (2013).

Author contributions

S.K., R.G. and A.K.S. conceived the project. S.K. designed and performed the experiments. S.G. and D.C. contributed towards handling and complete characterization of the bacteria. S.K., R.G. and A.K.S. analysed results. S.K., R.G. and A.K.S. wrote the paper with inputs from D.C. and S.G.

Additional information

Supplementary information is available in the online version of the paper. Reprints and permissions information is available online at www.nature.com/reprints. Correspondence and requests for materials should be addressed to A.K.S.

Competing financial interests

The authors declare no competing financial interests.

Methods

Bacterial strain and growth condition. *Bacillus licheniformis* (Weigmann 1898) Chester 1901 (also known as *B. licheniformis* ATCC 14580) was bought from Microbial Culture Collection at the National Centre for Cell Science, Pune, India (Catalog No.-MCC 2047). Bacteria were grown in Tartoff–Hobbs Hiveg broth (Himedia) at 37 °C with vigorous shaking. The suspension of bacteria was aliquoted for experiment at the sixth hour of growth in 5 ml of Tartoff–Hobbs Hiveg broth.

Laser trapping and particle position determination. The crosslinked poly(styrene/divinylbenzene) (P[S/DVB]) particles of 5 μm were obtained from Bangslabs, USA. The particles were trapped in a optical trap obtained by tightly focusing an infrared laser beam (NdYVO4 laser of wavelength 1,064 nm) with a ×100 (1.4 NA) objective mounted on a Carl Zeiss Axiovert Microscope. An extremely low power aligned red laser (Thorlabs ML101J8 Diode laser of wavelength 632 nm controlled using a Thorlabs TCLDM9 temperature-controlled laser diode module) is switched on during the isochoric process and is used as a marker to define the end points of the process with an accuracy within the limits of our temporal resolution (see Supplementary Movies 1 and 2). T_{bath} is tuned by flowing a heat exchanging fluid, in this case water, in a channel adjacent to the bacterial reservoir. The bacterial reservoir and the heat exchanging fluid are separated by a #1 (100 μm thick) glass coverslip for quick equilibration. Particles were imaged using a Basler Ace 180 kc colour camera at 500 frames/s. Only the green slice of the RGB image was considered so as to eliminate the influence of the red laser(632 nm) on the particle position. The particle was tracked to sub-pixel resolution using the tracking codes by R. Parthasarathy[30]. The particle positions could be determined with an accuracy of 10 nm.

Active Stirling cycle. A typical cycle executed by the engine is outlined in Fig. 1. The process starts at state point 1 where $T_C = 290$ K and trap stiffness $k = k_{min} = 11.5$ pN μm^{-1} (see Supplementary Fig. 4). Bacteria in this state are sluggish but still active. The probability distribution of displacements in the x-position, $P(\Delta x)$, of the colloidal bead corresponding to this state point is also shown. The error bars in the histograms represent standard error of the mean and are obtained from multiple realizations of the Stirling cycle for approximately the same ΔT_{act}. The black line is a Gaussian fit to the data and points outside the fit represent non-Gaussian displacements. The trap stiffness k is increased linearly to $k_{max} = 18.7$ pN μm^{-1}, analogous to a macroscopic isothermal compression, and the system reaches the state point 2. The increase in k results in a narrower $P(\Delta x)$. The bath temperature is increased to $T_H = 313$ K at $k = k_{max}$ and the system reaches state point 3. A substantial increase in the width of $P(\Delta x)$ due to enhanced bacterial activity during the isochoric heating is clearly evident (Fig. 1). k is decreased linearly to k_{min}, analogous to a macroscopic isothermal expansion, and the system reaches state point 4. Finally, by isochoric cooling to T_C, keeping $k = k_{min}$, the cycle returns back to state point 1. T_C and T_H are kept the same for the passive (no bacteria present) as well as the active engine for all activities investigated. The isothermal processes were executed in 7 s and isochoric processes in 4 s, and the time taken to complete one Stirling cycle, $\tau = 22$ s, was held constant (see Supplementary Information and Supplementary Fig. 4). The position of the colloidal bead represents the state of the system as the cyclic process described in Fig. 1 is steadily executed.

Quantifying the performance of Active Stirling engines. Thermodynamic quantities were computed from particle trajectories using the framework of stochastic thermodynamics[6,28]. The work done by the engine is $W = \int (\partial U/\partial t)dt$, where $U(x,t) = (1/2)k(t)x(t)^2$, with $x(t)$ being the displacement of the bead from the trap centre at time t. In this sign convention the work done, W, by (on) the

system on(by) the surroundings is negative(positive). W is non-zero during the isothermal processes (1 → 2 and 3 → 4) and zero in the isochoric processes (2 → 3 and 4 → 1). Heat transferred, Q, by the reservoir in the isothermal processes can be calculated using an energy balance reminiscent of the first law of thermodynamics, $DU = Q - W$, despite Q and W being fluctuating quantities[28]. The energy balance is observed to be true for our active engines as well (see discussion following equation 6 of Supplementary Information). In the isothermal processes $DU = 0$ and $Q = W$. Heat transferred during the isochoric processes is calculated using $Q = - \int (\partial U/\partial x)\dot{x}dt$ and, for constant k, results in a path-independent form for $Q = -(k/2) \left[x^2 \right]_0^t$. The efficiency of the engine is defined as $\mathcal{E}_{cycle} = W_{cycle}/Q_h$, where Q_h is the heat transferred in the isothermal expansion 3 → 4 and W_{cycle} is the work done at the end of the Stirling cycle. Since fluctuations in our system follow non-Gaussian statistics, T_{act} cannot be used to define thermodynamic quantities. As per the definition, T_{act} is the temperature of an equilibrium reservoir with the same average potential energy $\langle U \rangle$ as the trapped bead in our bacterial reservoir. Thus, the equilibrium reservoir at T_{act} and our bacterial reservoir transfer the same amount of heat during an isochoric process.

$\mathcal{P}$ for a heat engine is a non-monotonic function of τ. As $\tau \to 0$, a substantial amount of heat drawn from the hot reservoir is lost towards irreversible work, W_{irr}, and $\mathcal{P}$ is small since W is small. For large cycle durations ($\tau \to \infty$), that is, the quasistatic limit, while both W_{irr} and $\mathcal{P} \to 0$, $\mathcal{E}$ reaches its maximum as the heat drawn during the isotherms is completely converted to work. The performance of engines in this limit is described by equilibrium stochastic thermodynamics. For intermediate τ, however, a trade-off between W_{irr} and τ results in a maximum in $\mathcal{P}$ (refs 31,32). Thus, a comparison across engines is possible only at maximum $\mathcal{P}$ or in the quasistatic limit (maximum $\mathcal{E}$), where the nature of irreversibility is well understood.

Origin of non-Gaussian fluctuations. The non-Gaussian fluctuations of particles in active reservoirs is a result of the underlying bacterial motility. It was recently shown that a colloidal particle diffusing in an active bath in the absence of any confining potential shows super-diffusive behaviour for times smaller than a characteristic time, τ_c (refs 13,33). In our experiment, $\tau_c \sim 1s$ (see Supplementary Information and Supplementary Fig. 9), while the timescale over which the particle experiences the optical trap is of the order of 10 ms. Further, exact solutions[15] to the Langevin equation for a self-propelled particle in a harmonic trap suggests that the shape of $P(\Delta x)$ is determined by parameter $a = (2\mu k\tau_c)^{-1}$, where μ is the mobility of the particle. $P(\Delta x)$ shows Gaussian behaviour as $a \sim 1$, and becomes increasingly non-Gaussian in the limit $a \ll 1$. In our experiment, $a \sim 10^{-4}$ and $P(\Delta x)$ is strongly non-Gaussian. The Gaussian behaviour is recovered in the macroscopic limit of smoothly varying potentials ($k \to 0$) or large particle diameters ($\mu \to 0$). Thus, our observations arise as a consequence of operating the engine in a spatial and temporal regime that precedes the onset of an effective equilibrium.

Data availability. The data that support the plots within this paper and other findings of this study are available from the corresponding author upon request.

References

30. Parthasarathy, R. Rapid, accurate particle tracking by calculation of radial symmetry centers. *Nat. Methods* **9,** 724–726 (2012).
31. Schmiedl, T. & Seifert, U. Efficiency at maximum power: an analytically solvable model for stochastic heat engines. *Euro. Phys. Lett.* **81,** 20003 (2008).
32. Curzon, F. L. & Ahlborn, B. Efficiency of a Carnot engine at maximum power output. *Am. J. Phys.* **43,** 22–24 (1975).
33. Hatwalne, Y., Ramaswamy, S., Rao, M. & Simha, R. A. Rheology of active-particle suspensions. *Phys. Rev. Lett.* **92,** 118101 (2004).

A micrometre-sized heat engine operating between bacterial reservoirs

Sudeesh Krishnamurthy,[1] Subho Ghosh,[2] Dipankar

Chatterji,[2] Rajesh Ganapathy,[3,4] and A. K. Sood[1,3]

[1]*Department of Physics, Indian Institute of Science, Bangalore - 560012, INDIA*

[2]*Molecular Biophysics Unit, Indian Institute of Science, Bangalore - 560012, INDIA*

[3]*International Centre for Materials Science,*

Jawaharlal Nehru Centre for Advanced Scientific Research,

Jakkur, Bangalore - 560064, INDIA

[4]*Sheikh Saqr Laboratory, Jawaharlal Nehru Centre for Advanced Scientific Research,*

Jakkur, Bangalore - 560064, INDIA

(Dated: July 27, 2016)

I. BACTERIAL GRAM STAINING AND GROWTH CURVE DETERMINATION

A. Gram staining

Gram staining was done using Gram staining kit (Himedia) according to the protocol supplied by the manufacturer. Gram stained slide was viewed using 43X objective in a bright field microscope (Axio Scope. A1, Carl Zeiss). The cells were stained with violet colour indicating that the bacteria are gram positive.

B. Bacteria growth curve

B. licheniformis was grown in Tartoff-Hobbs Hiveg broth (Himedia). Aliquots of culture were taken out each hour till 8th hour, diluted in Tartoff-Hobbs Hiveg broth (Himedia) and plated on LB agar plates. The plates were incubated at 37°C and colonies on plates were manually counted. The growth curve obtained is plotted in Fig. S1. The dashed line in the figure indicates the growth stage when aliquots of the bacterial suspension were drawn for the experiment.

C. Active engine - experimental conditions

The experiment was performed in a cross flow cell arrangement consisting of two independent microfluidic channels perpendicular to each other and placed one above the other. The bacterial sample was filled in the bottom channel while heat exchanging fluid was circulated through the top channel. The channels were separated at the region of intersection by a thin glass wall which facilitates quick thermal equilibration of the bacterial sample with the heat exchanging fluid. The bacteria sample used in the experiment were aerobic in nature and are active only near an air-water interface [1]. We half-filled the bottom channel and maintained an air-water interface through which oxygen diffused into the solution to keep the bacteria alive. While the activity was observed to be highest at the interface [1], it remained constant to about $100 \mu m$ into the solvent before acutely decreasing to zero. Our experiments were performed in the region of constant activity. We observed that as the temperature of the bacterial sample was changed, the metabolism rate of the bacteria changed, which in turn affected the activity of the system. As documented earlier [2, 3], both swim velocity and
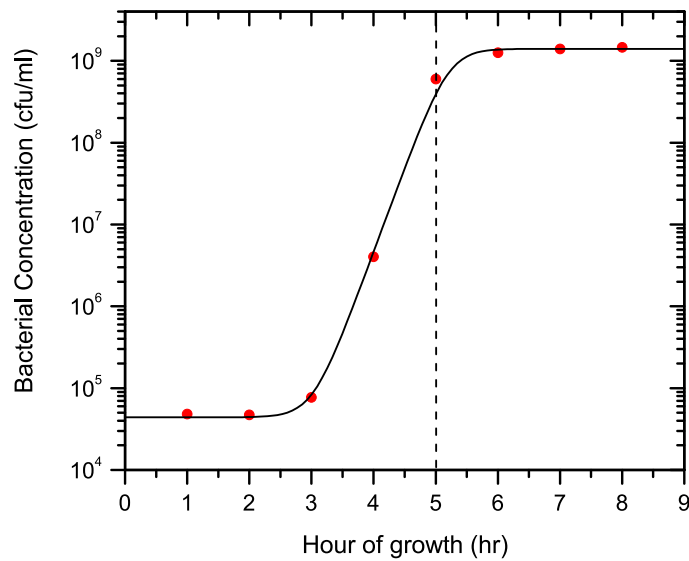
Fig. S 1. **Bacterial growth curve** Bacterial concentration(red circles) obtained by counting colonies in an inoculated plate at different stages of bacterial growth. The black line represents a Sigmoidal fit to the data. The bacterial samples used during the experiment were drawn at the transition to the stationary phase(dashed line).

persistence length of the bacterial motion vary with the bath temperature. The times spent by the bacteria in running and tumbling motion, however, remain the same.

To reduce bacterial death during our experiment, we maintained an oxygen saturated atmosphere at the air-water interface due to which the bacteria remained alive for about 2 hours. Nevertheless, since we are operating in the saturation regime of bacterial growth in order to maintain a constant number density, some bacterial cell death was inevitable.

D. Optical trapping of colloidal beads in the bacterial sample

The colloidal beads were suspended in the aliquots drawn from the bacterial sample and trapped by focusing an IR laser in the bottom channel. The colloidal beads were trapped $25\mu m$ above the base of the bottom channel in all our experiments. Bacterial samples used in the experiment contained a mixture of live and dead bacteria along with a few impurities. The refractive index of all these constituents were greater than the solvent and this resulted in simultaneous trapping of these impurities (in some instances also live bacteria) along
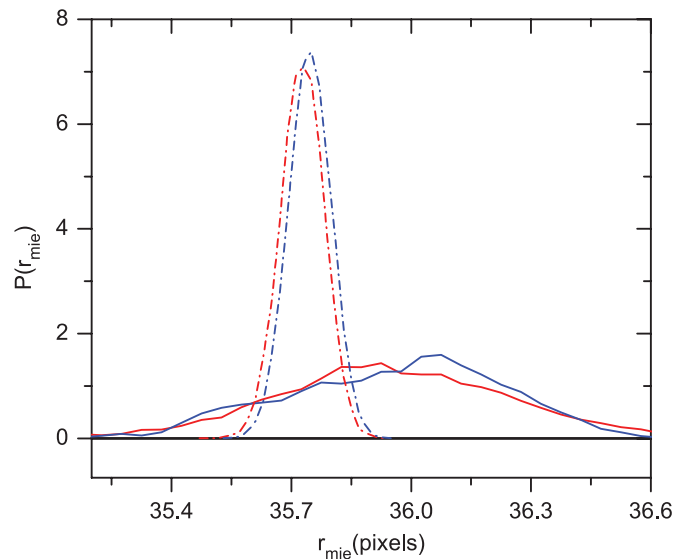
Fig. S 2. **Probability distribution of the first ring of the Mie patterns for colloidal beads in different reservoirs** Probability distribution of the Mie radius of colloidal beads trapped in Active (Solid lines) and Passive reservoirs (Broken Lines). The difference in the mean of the distribution for hot reservoirs (red lines) and cold reservoirs (blue lines) for the active case and the passive case were both found to be ≈ 0.02 pixels

with the colloidal bead. To avoid the trapping of impurities, glycerin was added to the bacterial sample to raise the refractive index of the solution. In our experiments, the Glycerol concentration in the solution was 10% v/v and this reduced both, trapping of the bacteria and attenuation of laser by the bacteria, while the bacteria were live and active at this concentration. However, due to their spread in the refractive indices, we observed trapping of impurities during some cycles of our experiment, albeit with a small trapping force.

To rule out the possible influence of the trapped bacteria on our experimental findings, we analysed the dynamics of the Mie interference pattern of the trapped colloid and compared it with a colloid trapped in a passive bath. The fluctuations in radius of the Mie rings are indicative of the fluctuations in the vertical direction (z-direction) of the trapped colloidal particle [4]. In Fig. S2, we show the probability distribution of radius of the first Mie ring for bead in passive and active reservoirs for hot and cold cycles, respectively. We find that, while mean positions of the Mie radius between active and passive reservoirs differ due to particle polydispersity, the difference between the hot and cold cycles remain the same in both the reservoirs. This confirms that the trapped bacteria did not influence the calculated

work done and efficiency.

Further, we compared the performance of the engine during the experimental cycles with(See supplementary video 3) and without bacterial trapping(See supplementary video 2). The results of the former were averaged over 34 and the latter over 20 cycles respectively. With the bacteria, $\langle W_{cycle} \rangle = -2.69 \pm 0.70 k_B T_C$ and $\langle \mathcal{E}_{cycle} \rangle = 0.44 \pm 0.11$. Without the bacteria, $\langle W_{cycle} \rangle = -2.78 \pm 0.82 k_B T_C$ and $\langle \mathcal{E}_{cycle} \rangle = 0.42 \pm 0.13$. We observe that the difference in work done and efficiency is indeed negligible and lies within the error bars of the experiment.

II. DETERMINATION OF EXPERIMENTAL PARAMETERS - BATH TEMPERATURE AND TRAP STIFFNESS

Precise measurement of thermodynamic quantities in our experiment requires determination of experimental control parameters, bath temperature(T_{bath}) and trap stiffness(k). Control over T_{bath} decides the time taken by the engine to execute the isochoric processes, t_{ic}. Estimating the precise value of k is vital to the evaluation of thermodynamic quantities. Further, the trap should be harmonic over the range of particle positions that are explored.

A. Control of bath temperature

The time taken by the sample to equilibrate with the heat exchanging fluid, in this case water, t_{eq} decides t_{ic} in our experiment. We used the temperature dependence of viscosity, η to estimate t_{eq} for our experiment. A 5 μm P[S/DVB] colloidal bead was trapped in the optical trap and dragged iteratively in a trapezoid velocity profile along the x-axis(Fig. S3a). Alternate cycles of hot and cold water were passed through the heat exchanging channel for 7s each as the bead is dragged through the sample. The displacement of the bead from the center of the trap, Δx is measured during the process. Fig. S3b shows $|\Delta x|$ as a function of time for such an experiment. η is known to decrease monotonically with the bath temperature. Thus, the drag force, $F_d = 6\pi\eta av = k\Delta x$ and the corresponding displacement Δx are lower when the sample is in contact with the hot reservoir. Fig. S3b shows regions of high and low $|\Delta x|$. The regions of high(low) $|\Delta x|$ correspond to cold(hot) water being circulated through the heat exchanging channel. t_{eq} is less than 1s (Fig. S3b).
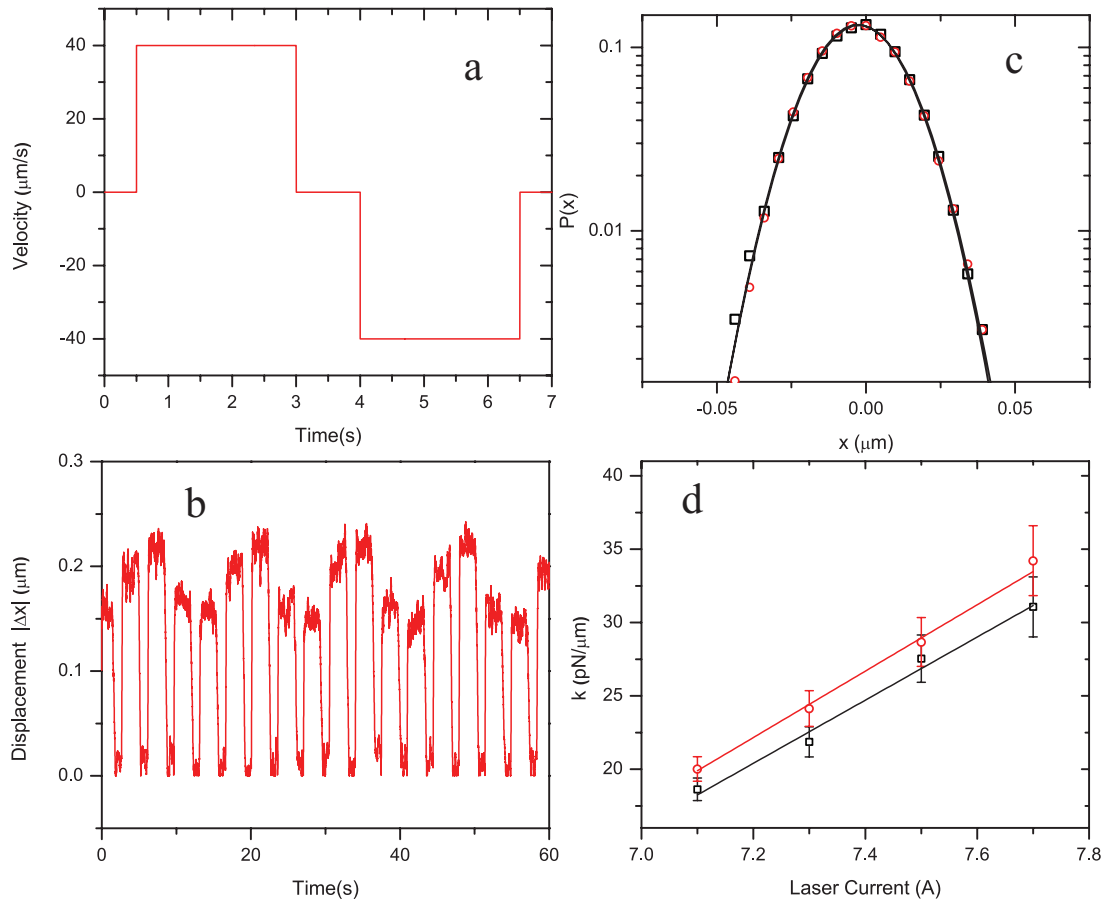
Fig. S 3. **a** & **b.** **Determination of** τ_{eq} **for the experimental setup** A colloidal particle is trapped in the media solvent and dragged by moving the optical trap along the x-coordinate in the velocity pattern shown in **a**. The resulting displacement from the centre of the trap ($|\Delta x|$), shown in **b**, is measured as alternate cycles of hot and cold water are passed through the heat exchanging channel. **c** & **d.** **Determination of** k **using equipartition theorem** $P(x)$ (open black squares) and $P(y)$ (open circles) for a trapped colloidal bead are shown in **c**. The black lines are Gaussian fits to the distributions and overlap on each other. Precise values of k_x (open black squares) and k_y (open red circles) determined at various Laser diode currents are plotted in **d**. The black(red) line represents the linear fit to the $k_x(k_y)$ at different diode currents.

In our experiment, we set t_{ic} at 4s. During this time we expect not just the equilibration of the sample (which happens within 1s) but also the associated flows to be reduced to zero.

B.   Determination of trap stiffness

To determine k, we used the equipartition theorem method. Fluctuations of a $5\mu m$ P[S/DVB] colloidal bead suspended in media solvent was studied under the influence of the trapping potential. The particle positions were measured over time intervals of 2 ms each while the velocity correlations decayed on a time scale two orders of magnitude less than our measurement. Fig. S4c shows $P(\Delta x)$ (Open squares) and $P(\Delta y)$ (Open circles) at the least k used in the experiment and the black lines are Gaussian fits for distributions. The trap is almost symmetric about x and y directions and the Gaussian fits for the $P(\Delta x)$ and $P(\Delta y)$ overlap ($\langle \Delta x^2 \rangle = 2.20 \times 10^{-4} \mu m^2$, $\langle \Delta y^2 \rangle = 2.09 \times 10^{-4} \mu m^2$). From the Gaussian fits in Fig. S3c, it is clear that the trap is harmonic. The trap stiffness, k can be evaluated using equipartition theorem, $\frac{1}{2}k_x \langle x^2 \rangle = \frac{1}{2}k_B T$. Fig. S3d shows the variation of k with diode current of the laser head. k varies linearly with the laser diode current in both x and y directions.

III.   PASSIVE MICROMETER-SIZED HEAT ENGINE

The micrometer-sized heat engine was tested with a passive reservoir for consistency with previous observations [7]. For clarity, we elaborate on the operation of the engine here. A 5 μm P[S/DVB] bead is suspended in water and is held in an optical trap. Stirling cycle as depicted in Fig. 1 of the paper is executed and the particle positions are measured. Fig. S4a shows total work done, W during individual cycles of the engine in contact with the passive reservoir. The cycle starts with isothermal compression where work is done by the surroundings on the system and $\Delta W > 0$ according to our convention. The process is represented by the blue shaded region of Fig. S4a and $\Delta W > 0$ as expected. The isochoric heating is not plotted since $W = 0$ during the process. During isothermal expansion, the system does work on the surroundings and $\Delta W < 0$ and is represented by the red shaded region of the Fig. S4a. The work done during isothermal expansion is larger than the work done in isothermal compression. This difference builds up as the engine is continuously operated and total work done steadily grows more negative as was shown in Fig. 2c of the main text.
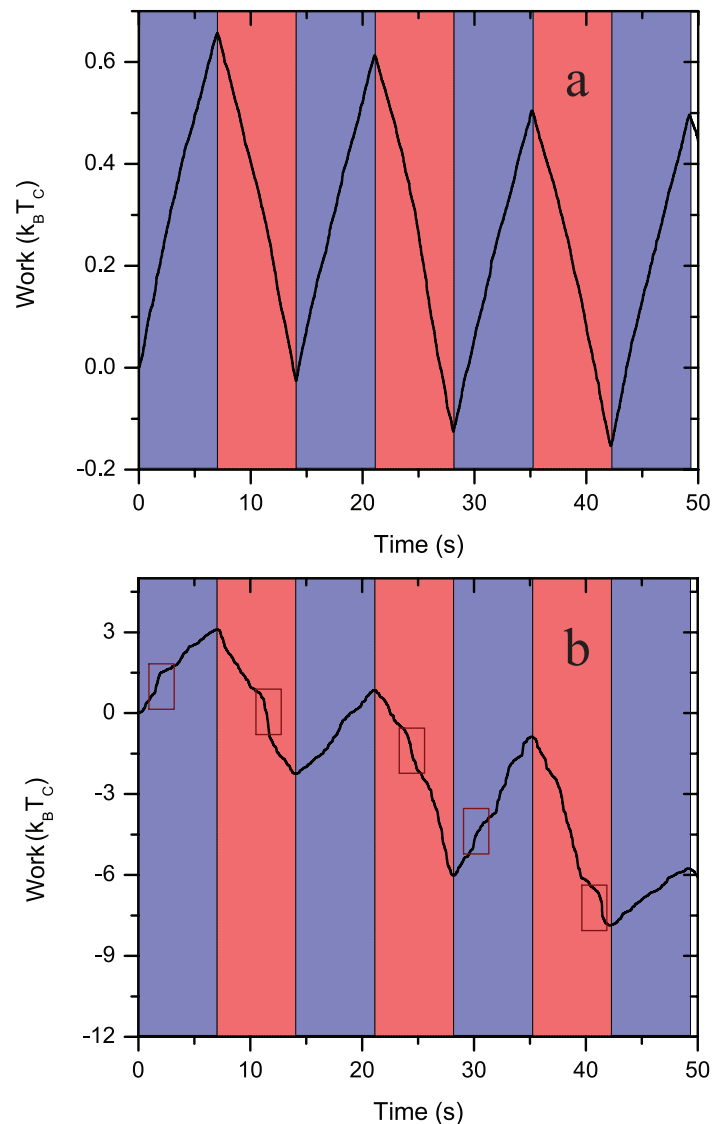
Fig. S 4. **Passive heat engine a.** Cumulative work done by the passive engine as the Stirling cycle is continuously executed. Red(Blue) shaded regions on the figure represent isothermal expansion(compression). Isochoric cycles are clipped from the time line as $W = 0$ during these processes. **b** shows fluctuations in work done by the engine in each completed Stirling cycle. **Active heat engine a.** Cumulative work done by the active engine as Stirling cycle is continuously executed. Similar to the passive engine, red(blue) shaded regions represent isothermal expansion(compression) and isochoric processes are clipped from the time line. Fluctuations in the work done with occasional large jumps (marked by brown squares) are more clearly visible.

IV.   ACTIVE MICROMETER-SIZED HEAT ENGINE

In our experiment, Stirling cycle was performed (similar to the passive heat engine) in an active bacterial medium. Here, we present raw data from our experiments where, the influence of fluctuations on the W_{cycle} of the engine becomes more apparent. Fig. S4b shows work done, W, as the engine executes various processes of the Stirling cycle. Isochoric processes where, $W = 0$ are clipped from the time series. Isothermal compression is represented by the blue shaded region where $\Delta W > 0$ as expected. However, fluctuations in W are more apparent in the active engine as compared to the passive one. A closer examination reveals regions of large jumps in W which corresponds to a few very large fluctuations where most of the work is done. Isothermal expansion is represented by the red shaded regions and $\Delta W < 0$. The difference between work done in isothermal expansion and isothermal compression is more starkly visible in the active engine. Such a difference arises from the huge contrast between the activity of hot and cold reservoirs.

V.   COMPARISON OF PERFORMANCE OF HEAT ENGINES

A.   Gaussian engine

In Fig 3 of the main paper, we compared the experimental active engine with a simulated Gaussian engine. To obtain the results for simulated Gaussian engine, we generated the trajectories by considering only the region within the Gaussian fit to $P(\Delta x)$. We generated values for Δx corresponding to this region using the Gaussian random number generator in MATLAB. A cumulative sum of these displacements yielded a trajectory that was subsequently used to calculate the performance of the Gaussian engine.

B.   Statistics of our experiments

Due to the stochastic nature of the experiment, the results presented in the main paper were averaged over multiple realizations as shown in the main paper. In Figs. S5 a and b, we show $\langle W_{cycle} \rangle$ and $\langle \mathcal{E}_{cycle} \rangle$ for these multiple realizations. The error bars of each realization corresponds to the standard deviation of the quantities. The results in the main paper were obtained by suitably grouping and averaging over these realizations as described in Figure
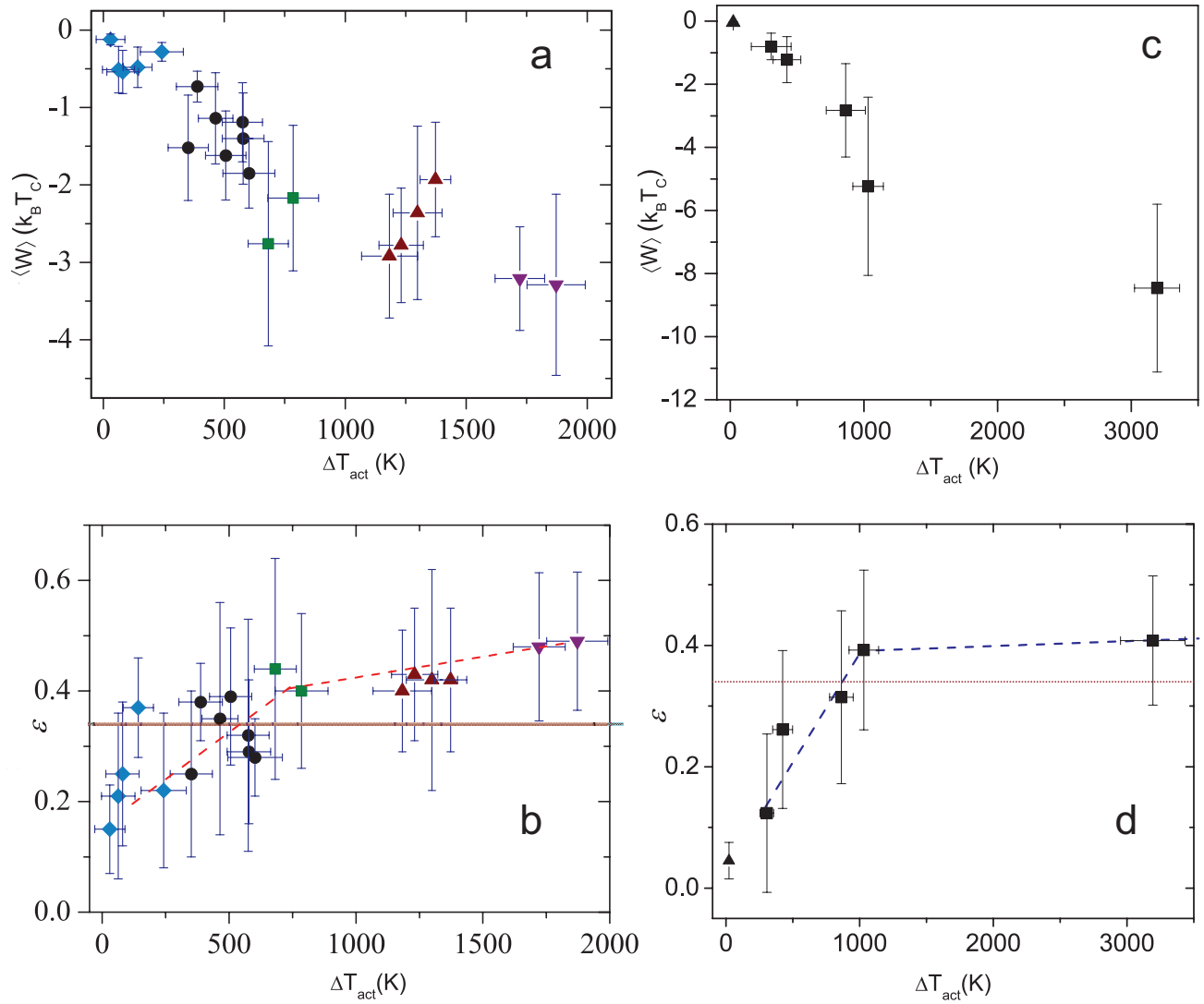
Fig. S 5. $\langle W_{cycle} \rangle$ **and** $\langle \mathcal{E}_{cycle} \rangle$ **for individual realizations of the engine** a and b show $\langle W_{cycle} \rangle$ and $\langle \mathcal{E}_{cycle} \rangle$ for individual realizations contributing to W and $\mathcal{E}$ calculated in the main paper. c and d show similar quantities calculated for engines with different trap stiffness maintaining the ratio k_{max}/k_{min} constant. The solid lines in b and d represent $\mathcal{E}_{sat}$

2b of the main paper and the error bars in the main paper correspond to the standard error in the mean.

To test the robustness of our results, we realized similar active engines at different trap stiffness keeping the ratio k_{max}/k_{min} constant. These experiments were performed with a different batch of broth and in the absence of oxygen saturation at the interface. This resulted in fewer cycles than those presented in the main paper. The results are presented in Figs. S5c and d. The dependence of $\langle W_{cycle} \rangle$ and $\langle \mathcal{E}_{cycle} \rangle$ on ΔT_{act} remains similar to that

presented in the main paper and reaffirms our results.

VI.   CALCULATION OF WORK DONE AND HEAT TRANSFERRED

We used the framework of Stochastic Thermodynamics [5, 6] to determine the work done and heat transferred during various cycles of the experiment. Work done is obtained by evaluating the integral

$$W = \int \frac{\partial U}{\partial t} dt \tag{1}$$

Since the optical potential created by the trap is harmonic,

$$U = \frac{1}{2} k_x x^2 + \frac{1}{2} k_y y^2 \tag{2}$$

Here, k_x and k_y are the trap stiffnesses along the x and y directions respectively. Work done is obtained by discretization of the integral in (1) using (2)

$$W = \frac{1}{\nu} \sum_0^t \frac{1}{2} \dot{k}_x x^2 + \frac{1}{2} \dot{k}_y y^2 \tag{3}$$

where, ν is the frequency at which the position of the particle is measured. From (3) it is clear that work done is finite during Isothermal processes ($\dot{k} = $ constant) and zero during Isochoric processes ($\dot{k} = 0$).

Heat transferred is determined by evaluating the integral,

$$Q = -\int \frac{\partial U}{\partial t} \dot{x} dt = -\int k_x x \dot{x} + k_y y \dot{y} dt \tag{4}$$

During the isothermal processes of the Stirling cycle, the trap stiffness is varied linearly and we have for isothermal expansion,

$$k = \frac{\Delta k}{\Delta t} t + k_{min} \tag{5}$$

Substituting into the integral in (4) and by integration by parts, we obtain heat transferred in the x degree of freedom, Q_x as

$$Q_x = -\left[k_{max} x(t)^2 - k_{min} x(0)^2 \right] + \frac{1}{2} \int_0^t \frac{\Delta k}{\Delta t} x^2 dt \tag{6}$$

For an equilibrium system, the first term in the RHS of (6) is zero during an isothermal process and by equipartition theorem.

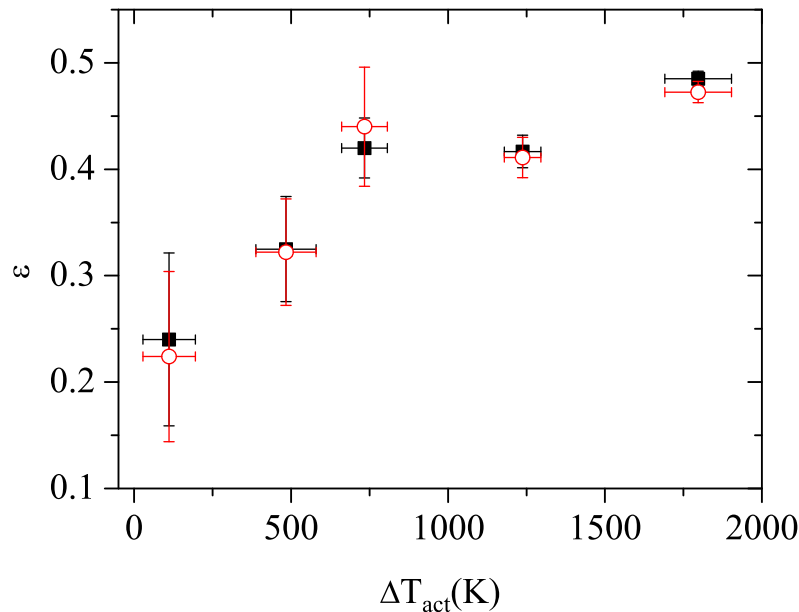$$k_{min} x(0)^2 = k_{max} x(t)^2 = k_B T \tag{7}$$

Fig. S 6. **Comparison of $\mathcal{E}$ calculated with and without accounting for the boundary term in equation 6** Red circles and Black squares represent $\mathcal{E}$ calculated with and without accounting for the boundary term respectively

For an active reservoir, the first term in (6) is not necessarily zero. $P(\Delta x)$ in Fig. 2a of the main text and Fig. S7 are rescaled maintaining $kx(0)^2 = kx(t)^2$. Since the rescaled $P(\Delta x)$ at various points along the isotherm fall on top of each other, the first term in (6) is on an average zero for the active reservoir. Neglecting this boundary term affects the calculation of efficiency of the engines whereas the work done remains unaffected. In Fig. S6, we calculate efficiencies with and without accounting for the boundary term. Nevertheless accounting for the boundary does not result in significant changes to the calculated efficiency, thus reaffirming our original results.

The second term in (6) is the work done by the engine in isothermal process. Thus, for the isothermal processes, heat transferred is equal to the work done in the process,

During an isochoric processes, the trap stiffness is constant and heat transferred can be calculated by evaluating the integral in 4.

$$
\begin{aligned}
Q &= -k_x \int_0^t x\dot{x}\,dt - k_y \int_0^t y\dot{y}\,dt \\
&= -\frac{k_x}{2} \int_0^t \frac{\partial x^2}{\partial t}\,dt - \frac{k_y}{2} \int_0^t \frac{\partial y^2}{\partial t}\,dt
\end{aligned}
\tag{8}
$$

Evaluating 8,

$$Q = -\frac{k_x}{2} \left[x^2 \right]_0^t - \frac{k_y}{2} \left[y^2 \right]_0^t \tag{9}$$

From equation (9), it is clear that the heat transferred during the isochoric processes depends only on the end points of the process.

VII.   ORIGIN OF NON-GAUSSIAN FLUCTUATIONS IN BACTERIAL RESERVOIRS

In the main text, we find that the superior performance of the active engine stems mainly from non-Gaussian fluctuations. Recent studies [8] have established that, such fluctuations arise in driven self-propelled media if the length scale of external driving potential varies on the same length scale as persistent motion. To extract the length and time scales associated with the persistent motion, we observe the dynamics of the colloidal bead in the absence of a driving potential. Fig. S7 shows mean square displacement of such a freely diffusing bead for different activities. The motion of the bead is superdiffusive on time scales less than a characteristic time $\tau_c \sim 1s$ and corresponds to a length scale $l_c \sim 2~\mu$m. At time scales larger than τ_c, the direction of motion randomizes and the particle exhibits diffusive motion. In our experiments, such a particle with mobility μ is confined in a harmonic potential of stiffness k. The particle experiences the potential on a time scale $\tau_{trap} = 1/f_T$, where f_T is the corner frequency of trapping potential. $f_T = k\mu/2\pi \sim 100Hz$ for the trap stiffness used in our experiments and $\tau_{trap} \sim 10ms$. Thus, the optical potential varies sharply on time scales associated with persistent motion. Following the exact solution [8] for a self-propelled particle in a harmonic potential, we calculated the parameter $a = (2\mu k \tau_c)^{-1}$ for our experiments. $a \sim 10^{-4} \ll 1$ for our experiments and the probability distribution is strongly non-Gaussian.
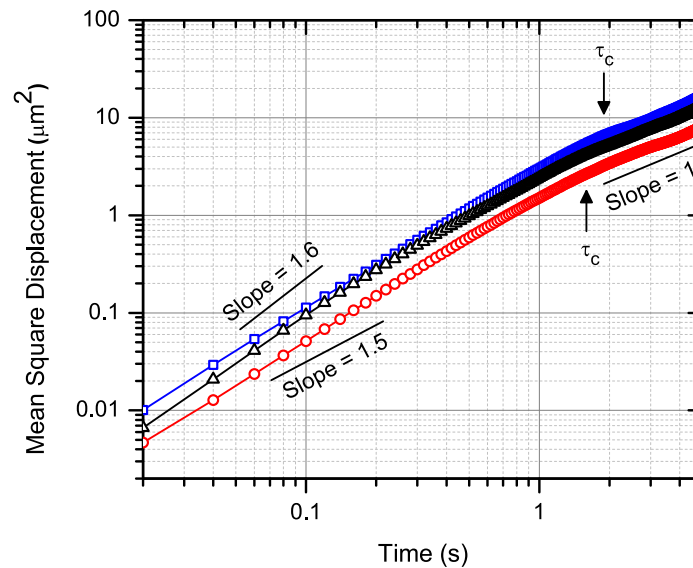
Fig. S 7. **Mean Square displacement (MSD) of a freely diffusing bead in a bacterial bath** MSD of a colloidal bead diffusing in the absence of an external potential for three different bacterial baths in ascending order of activity (red circles < black triangles < blue squares) are shown. Dynamics of the particle shows a crossover from superdiffusive(exponent ~ 1.55) to diffusive behavior(exponent ~ 1) at a characteristic time, $\tau_c \sim 1s$.

[1] Tuval, I. et.al. Bacterial swimming and oxygen transport near contact lines. *Proc. Natl Acad. Sci. USA.* **107**, 2277-2282 (2005)

[2] Shneider Jr.W. R. & Doetsch R.N. Temperature effects on bacterial movement. *Applied and Environmental Microbiology.* **34**, 6, 695-700 (1977)

[3] Lewis, P. & Ford, R. M. Temperature-sensitive motility of sulfolobus acidocaldarius influences population distribution in extreme environments. *J. Bacteriol.* **181**, 4020-4025 (1999)

[4] Lee, Sang-Hyuk .et.al. Characterizing and tracking single colloidal particles with holographic microscopy. *Optics Express*, **15**, 18275-18282 (2007)

[5] Sekimoto, K. Langevin equation and thermodynamics. *Prog. Theor. Phys. Suppl.* **130**, 1727 (1998).

[6] Seifert, Udo. Stochastic Thermodynamics, Fluctuation theorems and Molecular Machines. *Rep. Prog. Phys.* **75**, 126001 (2012).

[7] Blickle, V & Bechinger, C. Realization of micrometer sized stochastic heat engine. *Nature Phys.* **8**, 143-146 (2012).

[8] J. Tailleur & M. E. Cates . Sedimentation, trapping, and rectification of dilute bacteria. *Euro. Phys. Lett.* **86**, 60002(2008)